OPEN ACCESS
IOP Publishing
Nanotechnology

Nanotechnology **35** (2024) 175707 (11pp) https://doi.org/10.1088/1361-6528/ad2156

Transition from fractal-dendritic to compact islands for the 2D-ferroelectric SnSe on graphene/Ir(111)

P Aleksa[1], M Ghorbani-Asl[2], S Iqbal[1], M A Martuza[1], A Bremerich[1], D Wilks[1], J Cai[1], T Chagas[1], R Ohmann[1], A Krasheninnikov[2,3] and C Busse[1]

[1] Department Physik, Universität Siegen, D-57072 Siegen, Germany
[2] Institute of Ion Beam Physics and Materials Research Helmholtz-Zentrum Dresden-Rossendorf D-01328 Dresden, Germany
[3] Department of Applied Physics, Aalto University, PO Box 11100, FI-00076 Aalto, Finland

E-mail: paulus.aleksa@uni-siegen.de

Received 4 December 2023, revised 20 December 2023
Accepted for publication 22 January 2024
Published 9 February 2024

Abstract

Epitaxial growth is a versatile method to prepare two-dimensional van der Waals ferroelectrics like group IV monochalcogenides which have potential for novel electronic devices and sensors. We systematically study SnSe monolayer islands grown by molecular beam epitaxy, especially the effect of annealing temperature on shape and morphology of the edges. Characterization of the samples by scanning tunneling microscopy reveals that the shape of the islands changes from fractal-dendritic after deposition at room temperature to a compact rhombic shape through annealing, but ripening processes are absent up to the desorption temperature. A two-step growth process leads to large, epitaxially aligned rhombic islands bounded by well-defined ⟨110⟩-edges (armchair-like), which we claim to be the equilibrium shape of the stoichiometric SnSe monolayer islands. The relaxation of the energetically favorable edges is detected in atomically resolved STM images. The experimental findings are supported by the results of our first-principles calculations, which provide insights into the energetics of the edges, their reconstructions, and yields the equilibrium shapes of the islands which are in good agreement with the experiment.

Supplementary material for this article is available online

Keywords: groupIV-monochalcogenides, molecular-beam epitaxy, STM, SnSe, ferroelectricity, DFT, ripening processes

1. Introduction

Ferroelectrics have a spontaneous electrical polarisation below their critical temperature T_C, which can be reoriented by an electric field. Thin ferroelectric films are used in numerous applications as non-volatile memory, sensors, actuators, and optoelectronic devices [1, 2]. The ongoing trend in miniaturisation and increasing energy efficiency makes it desirable to reduce the thickness of ferroelectric films. However, for conventional ferroelectrics T_C falls below feasible values in thin films due to the intrinsic surface-charge-induced depolarisation field [3]. This is not the case for two-dimensional materials (2DMs) with in-plane ferroelectricity. For 2DMs, T_C above room temperature (RT) has been demonstrated in a ground-breaking study by Chang *et al* [4]. The polarisation of 2DMs is confined in the 2D-plane, and there can be no surface charges in the form of dangling

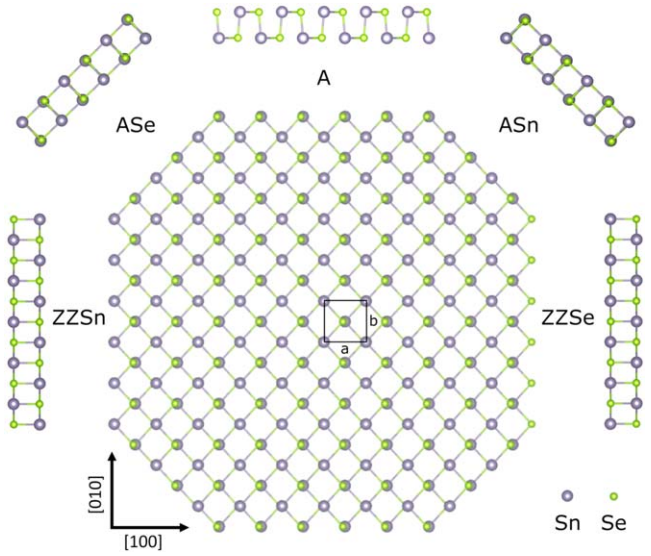

Figure 1. Crystal structure of freestanding monolayer SnSe (from our DFT calculation, see below). Purple balls represent Sn, green Se atoms. A unit cell with lattice constants a and b is indicated. We depict an island with all possible dense-packed edge types as cut from the infinite 2D lattice. Edges are labelled according to structure (A for armchair, ZZ for zigzag) and termination (Sn or Se), see text. Each different edge is represented with a side view.

bonds due to the layered crystal structure of the parent bulk materials. In general, 2D ferroelectricity is of equal interest as 2D ferromagnetism, yet more stable (as evidenced by the much higher T_C) for materials discovered up to now.

A prominent class of 2D-ferroelectrics are monolayered group-IV monochalcogenides with the structural formula MX (M = Ge, Sn; X = S, Se, Te) [5, 6]. In the following the term MX as well as the names of the individual compounds (as SnSe) will be used as shorthand for monolayers of the materials unless explicitly stated otherwise. Single MX layers are puckered sheets with a phosphorene-like orthorhombic structure [7], see figure 1, with a lack of inversion symmetry, which is mandatory for ferroelectricity. Specifically, the mutually tilted Sn–Se dipoles in the unit cell add up to the in-plane polarisation. Above the transition temperature this tilting vanishes, Sn and Se are vertically stacked on top of each other, and the net polarisation becomes zero.

Theory confirms particularly strong ferroelectricity for this family [8–11]. They are semiconductors, therefore switching can be integrated into logic circuits within one material. Despite a significant number of theoretical works [8–11], experimental studies are still scarce, which can be attributed to the difficult preparation of these systems [12].

MX monolayers are ideal materials for non-volatile memory devices, and prototypes based on ferroelectric tunneling junctions have already been realized [4]. Following this demonstration, sophisticated designs as the in-plane ferroelectric tunnel junctions have been proposed [13], which are non-volatile memory devices with low power usage that enables fast writing and reading with a nondestructive reading process.

There are several methods to obtain SnSe nanomaterials as recently reviewed by Li *et al* [14], including the preparation of thin films by chemical vapor deposition, physical vapor deposition, and pulsed laser deposition. However, the only method up to now that has been successful in the preparation of monolayers is molecular beam epitaxy (MBE) with its highly controlled conditions such as ultra-high vacuum and well-defined substrate [12, 15]. Beyond SnSe, epitaxial growth of SnTe [4], and SnS [16] has been demonstrated. The reports on GeSe are ambiguous [12], and preparation of GeS and GeTe has not yet been described.

While it can be expected that the other deposition methods mentioned above can be further refined to enable preparation of SnSe monolayers, more basic and potentially high-yield methods as mechanical or liquid phase exfoliation face the fundamental problem of the comparatively high exfoliation energy of bulk SnSe in particular and all MX in general [12, 14].

In MBE, MX powder or granules can be used as the source material, which simplifies the process compared to other binary compounds that require two sources. Epitaxial growth also enables the preparation of nanostructures as nanometre-scaled islands with ferroelectric properties being dependent on island shape and size as detailed in section 2.

Graphene emerged as a highly suitable substrate due to its quality, chemical inertness, and low charge carrier density [4, 12, 15]. In addition, this semimetallic substrate allows application of surface science methods. The studies mentioned above used graphitized SiC(0001). Our choice for the substrate is graphene on Ir(111) which is easy to prepare in a self-limiting (single layer only) process [17] and allows further tuning of the overlayer by contactless chemical doping [18].

An atomic-scale understanding of thin-film growth can enable rational tuning of preparation protocols to achieve desired morphologies. We expect that the rate ν of all relevant atomic mechanisms follow the universal Arrhenius law for thermally activated processes

$$\nu = \nu_0 \mathrm{e}^{-\frac{E_\mathrm{a}}{k_\mathrm{B}T}},$$

where ν_0 is the attempt frequency, E_a is the energetic activation barrier specific for the process, k_B is Boltzmann's constant, and T is the temperature. The understanding of atomic processes including the significance of individual mechanisms and even a quantification of their relevant parameters is highly developed for the most fundamental case of metal homoepitaxy [19]. However, for epitaxial growth of 2D-materials this field is much less advanced, and specifically for MX monolayers there are no studies on atomic processes during growth.

When shape or size of an island changes in annealing, this must be due to specific atomic processes: The shape can become more compact when there is effective step edge diffusion, the island can shrink when there is effective step atom detachment. In the general case the associated energy barriers will be different, leading to a hierarchy of processes and hence a complex dependence of the island morphology on annealing temperature. Often, different regimes in the

temperature dependence can be distinguished [19] as the exponential dependence of the rate ν on E_a activates different processes sequentially. To give an example: at the experimentally relevant temperature of 500 K (see below), for two processes with a difference in activation energy of only 0.2 eV, the one with the low barrier already happens 100-times faster than the one with the high barrier.

In this work, we describe the epitaxial growth of SnSe on graphene on Ir(111), where the islands evolve from fractal-dendritic to compact rhombuses with increasing temperature. We establish the hierarchy of key atomic processes (step edge diffusion, step atom detachment, desorption) relevant for nucleation, growth, and compaction. We study the morphology of the edges using first-principles calculations and find that relaxations play an important role in this system. The resulting equilibrium shape of the islands is in agreement with the experimental one. Atomically-resolved scanning tunneling microscopy (STM) images directly evidence the edge relaxation.

2. Theoretical background

For finite systems the electric polarisation $\vec{P}$ is the dipole moment $\vec{p}$ per island volume V_{island}, where $\vec{p}$ can be derived from the charge density distribution $\rho(\vec{r})$ [20]:

$$\vec{P} = \frac{\vec{p}}{V_{\text{island}}} = \frac{1}{V_{\text{island}}} \int_{\text{island}} \vec{r}\rho(\vec{r})\mathrm{d}\vec{r}.$$

Note that this approach fails for the polarization of an infinite system, where instead the modern theory of polarisation has to be used [20].

For the sake of illustration, we approximate our islands (that are of finite size) by a system of point charges q_i at positions $\vec{r}_i$. The integral above can then be written as a sum:

$$\vec{P} = \frac{1}{V_{\text{island}}} \sum_i \vec{r}_i q_i.$$

We can group the point charges into pairs consisting of an Se and an Sn atom slightly tilted out of the [100]-direction. By symmetry, the in-plane component of the dipole moment of each pair is the same. When it is possible to virtually separate the island into such pairs only, the resulting in-plane component of the polarization $\vec{P}_\parallel$ is independent on island shape and size (given that the out-of-plane components of neighbouring pairs will cancel out, $\vec{P}_\perp \approx 0$ for all but the smallest islands and hence $\vec{P} \approx \vec{P}_\parallel$). This, however, is only possible when the island is exclusively terminated by specific types of edges, see figure 1.

We denote the edges by the crystal directions perpendicular to them pointing outward. For the sake of illustration, we just cut the edges from the 2D infinite crystal and preserve stoichiometry for now. Due to the low symmetry of the crystal structure (only mirror symmetry with respect to [100]), there are 5 different types of close-packed edges (see also reference [21] for a detailed discussion and an explanation of the nomenclature). [010]- and [0$\bar{1}$0]-steps are equivalent, the atoms are found in an armchair-like structure (labelled A), and both types of atoms have the same distance from the step edge, making this edge charge neutral. The second pair is [110] and [$\bar{1}$10], which are also of armchair type, but the Sn atoms are closer to the step edge (ASn), making the step slightly positively charged. The counterpart are [1$\bar{1}$0] and [$\bar{1}\bar{1}$0] (ASe) which are slightly negative. Finally, [100] is exclusively terminated by Se in a zigzag arrangement (ZZSe), complemented by [$\bar{1}$00] (ZZSn). These step edges are strongly charged. Only in the absence of zigzag edges one can pair Sn and Se as introduced above. Otherwise, individual positive point charges (Sn) are left on one side and negative point charges (Se) are left on the other side. This results in a contribution to $\vec{P}_\parallel$ in the opposite direction to the one from the pairs, which in addition scales with the length of the edges and their separation. In consequence, the polarization of an island will depend on its shape and size. This necessitates a study of the geometry of islands as carried out in this work as a prerequisite for future analysis of ferroelectric properties.

3. Materials and methods

Samples were prepared *in situ* in an ultra-high vacuum system (VT-STM, Scienta Omicron) with a base pressure of 1×10^{-10} mbar. Sample temperature was measured by a pyrometer (Impac IGA140, Advanced Energy). A clean Ir(111) surface was prepared by 1.0 keV Ar^+ bombardment at RT and subsequent annealing at 1500 K. A closed monolayer of graphene (gr) was grown via a two-step process [17]: temperature programmed growth with exposure to 12 L ethylene at RT followed by thermal decomposition at 1400 K for the formation of well-oriented graphene nuclei, and then chemical vapor deposition to grow a complete layer through exposure to 120 L ethylene at 1250 K. Cleanliness of Ir(111) and high quality of gr/Ir(111) was verified by well-defined low-energy electron diffraction (LEED) patterns. SnSe (5 N powder, Alfa Aesar) was evaporated from an effusion cell (Kentax 3-cell evaporator). During evaporation, there were peaks stemming from SnSe-pairs as well as individual Sn and Se in the mass spectrometer. We cannot determine whether the SnSe-pairs dissociate only during detection or already partially during evaporation. The first increase in these peaks is observed at a crucible temperature close to 600 K, indicating the onset of evaporation. For a sufficient and stable rate we used 723 K. The rate was varied by changing the distance between source and sample from 8 to 12 cm. Evaporation rates were determined by STM. We define one monolayer (ML) as a complete single layer of SnSe, as depicted in figure 1. We did not observe any visual change in the source material remaining in the crucible even after long term use.

The samples were loaded into the STM housed in the same system. Such a transfer without breaking the vacuum is mandatory as we found that SnSe is unstable even under short exposure to ambient conditions. This is in line with the conclusion drawn in [14] from several studies that SnSe nanostructures oxidise in a normal environment.

STM measurements were conducted at RT. Images were calibrated by using the known lattice parameters of gr/Ir(111)

and its moiré superstructure [22]. Growth (evaporation rate, duration, sample temperature) and tunneling parameters (image size, bias voltage, tunneling current) are given for each image. All data were analysed using the WSxM software [23].

Density functional theory (DFT) calculations were performed using the Vienna *ab initio* simulation package (VASP) [24, 25]. The exchange-correlation functional was employed in the generalized gradient approximation of Perdew–Burke–Ernzerhof (GGA-PBE) [26]. An energy cut-off of 600 eV for plane-wave expansion was used for the primitive cell and 400 eV for supercell calculations, respectively.

The simulation models of edges were constructed using ribbons with various sizes ranging from 10×2 to 44×2 supercells for [100]- and $[\bar{1}00]$-edges, 10×2 to 45×2 supercells for [010]- and $[0\bar{1}0]$-edges, and ribbons with sizes of 7×2 to 32×2 supercells for [110]- and $[\bar{1}\,\bar{1}0]$-edges.

The Brillouin zone of the primitive cells and supercells were sampled using $(12 \times 12 \times 1)$ and $(4 \times 1 \times 1)$ Monkhorst–Pack k-point, respectively. All structures are fully optimized until the maximum force on each atom is less than 0.01 eV Å^{-1}. To check for consistency we calculated the optimized bulk structure and obtained lattice constants within 2% of experimental results [27].

Edge energy (eV Å^{-1}) is calculated as the difference between the ribbon with two edges and the periodic slab structure and normalized to the edge length L for each edge:

$$\delta = (E_{\text{ribbon}} - E_{\text{slab}})/2L.$$

Cohesive energy E_{coh} (eV/atom) is calculated as the difference between the energy of atoms in the 2D infinite SnSe crystal with respect to the number n and chemical potential μ of the isolated atoms:

$$E_{\text{coh}} = (E_{\text{SnSe}} - n_{\text{Sn}}\mu_{\text{Sn}} - n_{\text{Se}}\mu_{\text{Se}})/(n_{\text{Sn}} + n_{\text{Se}}).$$

Constant current STM images were simulated using the Tersoff-Hamann approximation. We incorporated all states up to 1.2 eV above the highest occupied state as we estimate this to be the best match to the experimental image taken at a bias voltage of 1.0 V.

4. Results and discussion

Evaporation of SnSe for 30 s with a rate of 5.2×10^{-3} ML s^{-1} on gr/Ir(111) at RT led to the morphology shown in figure 2: large, widely separated fractal-dendritic monolayer islands that are centered at pre-existing step edges or defects. Imaging was demanding as we had to use (i) low currents to prevent manipulation of the islands during scanning and (ii) high voltages due to the semiconducting nature of SnSe. The sample coverage was $\Theta_0 = (0.16 \pm 0.03)$ ML, the island density (determined by counting islands in many individual images) was $n_0 = (1.8 \pm 0.3) \times 10^{-8}$ Å^{-2}. We found an apparent island height of $h = (5.50 \pm 0.06)$ Å which did not depend significantly on tunneling parameters. The LEED image (inset) shows pronounced reflexes from gr/Ir (111) for large scattering vectors and weak reflexes from SnSe at small scattering vectors, indicating that the SnSe layer is crystalline after evaporation at RT. A full description of the diffraction pattern is postponed to figure 4 where the LEED image is clearer due to a higher SnSe coverage.

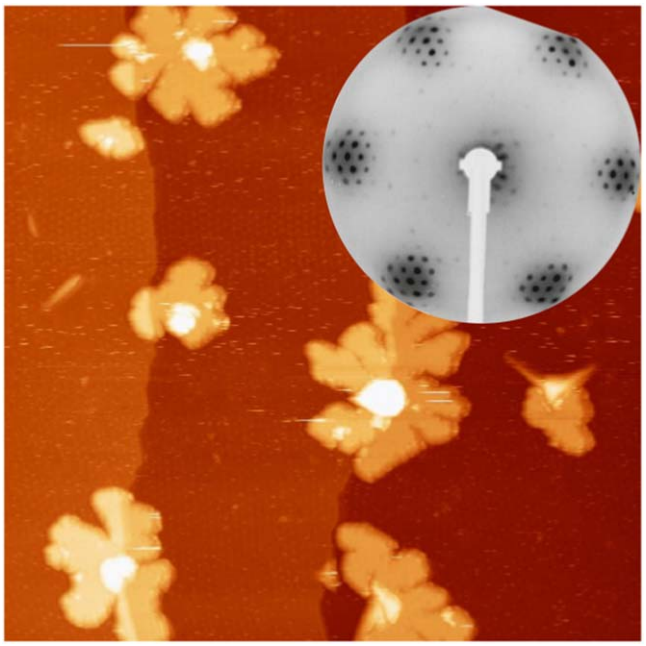

Figure 2. STM image of fractal-dendritic SnSe islands on gr/Ir(111); 5.2×10^{-3} ML s^{-1}, 30 s, RT; 1750 Å × 1750 Å, 3 V, 10 pA. Inset: LEED image (inverted contrast) measured at 74 eV.

The low island density indicates that the precursors for growth are rather mobile on gr/Ir(111) at RT and/or that nucleation is a process with a low probability. The ease of manipulation with the STM tip indicates a weak interaction between the 2DM and its substrate. The fractal-dendritic shape implies that step-edge diffusion is hampered. Inherent in this shape, the relative edge length is high and geometrically also has to contain the strongly charged zigzag edges. In consequence, for these fractal-dendritic islands we expect a strong impact of the steps on the overall polarization.

A measure for the shape of an island is the ratio between its perimeter and area A. As the perimeter is difficult to determine and conceptually also depends on the resolution of the underlying STM-image, we substitute it by the proportional and more robust experimental parameter A_{edge} that we define as the area in the height interval $[h - \Delta h_1, h - \Delta h_2)$, with $\Delta h_1 = 0.7$ Å and $\Delta h_2 = 0.2$ Å. An extended explanation is provided in figure S2 in supplementary material. By this, we derive the phenomenological shape parameter $A_{\text{edge}}/A = 0.121 \pm 0.004$. Alternatively, the fractal-dendritic islands can be characterized by their average branch thickness, which is (100 ± 30) Å in our case.

Upon annealing (1200 s on each step) the sample morphology changed, see figure 3. A representative STM image of an island after selected heating steps is presented in figure 3(a), an extended data set is provided in figure S1 in supplementary material. We characterize the changes in the morphology of our samples with temperature by three key

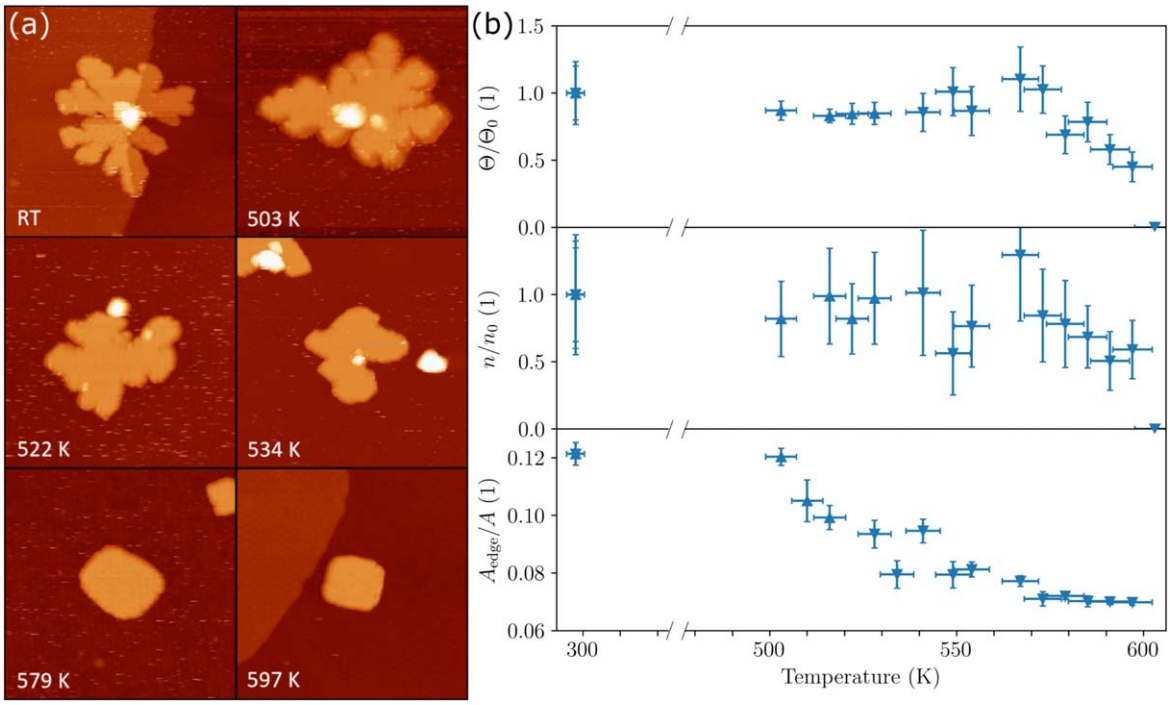

Figure 3. Annealing sequence. (a) STM images of SnSe/gr/Ir(111) (750 Å × 750 Å, 1−3 V, 5−10 pA) annealed after growth (5.2×10^{-3} ML s^{-1}, 10−30 s, RT) at the indicated temperature for 1200 s. We see an evolution from fractal-dendritic to compact islands. (b) Normalized coverage Θ/Θ_0 (top), normalized island density n/n_0 (middle) and shape parameter A_{edge}/A (bottom) in dependence of annealing temperature. Normalization: coverage ($\Theta_{0,\blacktriangle} = 0.16$ ML, $\Theta_{0,\blacktriangledown} = 0.08$ ML) and island density ($n_{0,\blacktriangle} = 1.8 \times 10^{-8}$ Å^{-2}, $n_{0,\blacktriangledown} = 1.1 \times 10^{-8}$ Å^{-2}).

parameters: coverage Θ, island density n and shape parameter A_{edge}/A, see figure 3(a). We analyzed 20–40 islands for each temperature step. The error for each parameter is the standard deviation between different images for Θ and n and between different islands for A_{edge}/A. The error in temperature stems from the uncertainty of the pyrometer. We conducted several annealing sequences, including a variation of the initial coverage Θ_0 between 0.08 and 0.16 ML (indicated by different symbols in figure 3 (b)), but found no differences in the behaviour of the morphological parameters. Therefore, we normalize both Θ and n by their initial values and combined all series in the graphs.

In the large temperature interval from 298 to 567 K, both the coverage and the island density did not change significantly, see top and middle panel in figure 3(b). This indicates that atoms do not detach from the step edges as this would lead to ripening (Ostwald ripening) via an adatom gas and/or to irreversible desorption of material from the substrate. At 574 K both coverage and island density start to decrease until at 603 K the SnSe-layer disappeared completely. This is in line with our observation that evaporation from SnSe powder starts at 600 K. The average island size ($\bar{A} = \Theta/n$) did not change over the whole temperature range, which also excludes ripening through island diffusion and coalescence (Smoluchowski ripening). This implies that the island disappear one after the other, which could be due to a critical step in the dissolution process of an island with a high activation barrier.

Even though islands do not interact with each other, there is a significant change in shape long before desorption sets in: already at 511 K the ratio of perimeter to area started to drop. We attribute this compaction to the onset of step edge diffusion. Due to the absence of ripening, we can exclude an exchange process through an adatom gas as the underlying mechanism. The compaction is completed at 574 K, i.e. before large changes in coverage and island density took place. The shape does not change upon further heating, so we postulate that here the islands obtained their equilibrium shape, which is a rhombus with rounded corners. As this shape is reached without any ripening, we conclude that at around 574 K each island is in local thermal equilibrium with itself. The SnSe-islands depicted in [15] obtained by an analogous preparation show a similar shape.

For epitaxial 2D materials on weakly interacting substrates as SnSe on gr/Ir(111) studied here, the bond strength within the layer is much larger than the one to the underlying material. In consequence, it is plausible that each atom or group of atoms that detaches from a 2D island will subsequently desorb from the substrate, which prohibits ripening processes during annealing. We propose that this is a general mechanism.

For future characterization of structural and electronic properties of SnSe islands, including the ferroelectric behaviour, a high coverage of large, well-separated islands with defined shapes and orientations is desirable. However, increasing the initial coverage in our experiments results in a

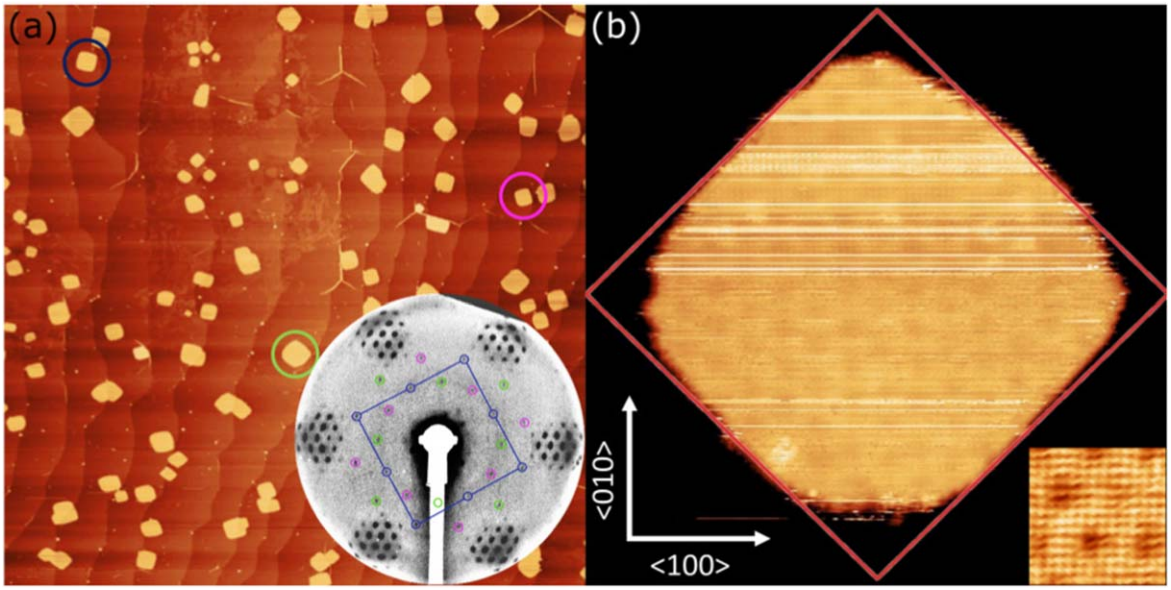

Figure 4. Orientation and equilibrium shape of SnSe/gr/Ir(111). (a) Overview STM image (17 500 Å × 17 500 Å, 3 V, 20 pA) with LEED (73 eV, inverted contrast) inset showing SnSe aligned to gr and marked in corresponding colours, grown in a two-step process at 5.2×10^{-3} ML s^{-1} for 60 s at RT and 1.72×10^{-3} ML s^{-1} for 600 s at 570 K. (b) STM image showing an equilibrium SnSe island; 5.2×10^{-3} ML s^{-1}, 10 s, RT and subsequently annealed at 570 K; 400 Å × 400 Å, −0.1 V, 200 pA; with atomically resolved inset; 5.2×10^{-3} ML s^{-1}, 30 s, RT and 1.72×10^{-3} ML s^{-1} for 300 s at 570 K; 60 Å × 60 Å, 1 V, 200 pA. In this panel, we rotated the measured topographs to align the lattice with the image. The red rhombus marks the expected equilibrium shape, see text.

high island density and nucleation of SnSe in the second layer. To avoid this, we introduced a two-step process: First, the formation of small rhombic islands as described above, which are subsequently expanded by a second deposition step at elevated sample temperature.

The STM image in figure 4(a) displays several SnSe islands together with different kinds of defects on the substrate: pre-existing-substrate steps, graphene wrinkles [28], and areas with a diffuse appearance that we attribute to intercalation [18, 29, 30]. Intercalation was only observed when SnSe was deposited at elevated temperatures.

The LEED image (inset of figure 4(a)) corresponding to the STM image and depicted in the same orientation shows a sixfold pattern of a group of reflexes at larger scattering vectors. Each group is built from a first order Ir(111) and a first order graphene spot, surrounded by satellite reflexes from the moiré superstructure. Closer to the center we observe 24 first order SnSe spots, which can be sorted in three groups of 8 spots (marked magenta, green and blue). Each group can be attributed to an orthorhombic lattice as exemplified for the blue spots by the blue lines. The [010]-direction of SnSe is aligned with the zigzag $\langle 11\bar{2}0\rangle$-direction of graphene. We determined the lattice constants as $a = (4.35 \pm 0.03)$ Å and $b = (4.26 \pm 0.02)$ Å. These values are identical to those found for SnSe on graphitized 6H-SiC(0001) [15].

There are six equivalent $\langle 11\bar{2}0\rangle$-directions that the SnSe lattice can align with. As SnSe possesses no rotational symmetry around the *c*-direction, this leads to six domains of SnSe/gr/Ir(111). However, they are related to each other by inversion in pairs of two. As diffraction is insensitive to this according to Friedel's law, this leads to our observation of three groups of spots.

All SnSe islands have very similar shapes which is a further indication that they are in thermal equilibrium. A well-formed island is shown in 4 (b). A superstructure is visible on the islands with identical lattice parameters as the gr/Ir(111) moiré superstructure [22] (which itself is faintly visible in the background of figures 2 and 3 (a)). In consequence, we interpret the superstructure of SnSe/gr/Ir(111) as the gr/Ir (111) moiré shining through the ultrathin overlayer, as previously observed for related systems [18, 31].

In atomically resolved images (inset of 4(b)) we observe protrusions that form a primitive lattice with the same parameters as determined by LEED within our error bars. This indicates that we only observe one of the four atoms in the primitive unit cell.

Given the strongly buckled structure of SnSe, it is expected that the atoms closer to the substrate are not visible in STM. The fact that we only see every other atom of the upper ones has to be due to differences in the local density of states, which is the parameter that STM is sensitive to. Following the arguments from Frezza *et al* (obtained from a comparison between non-contact atomic force microscopy (ncAFM) and STM measurements of SnSe/Au(111)) [32] we propose that we observe the lattice formed by the upper Sn atoms (as indicated by the unit cell in figure 1). This is supported by our STM simulations, see figure 6.

As we only observe one out of the four atoms in the unit cell, we can neither distinguish between [100] and $[\bar{1}00]$ nor between [010] and $[0\bar{1}0]$ using STM. In the following we will therefore use a slightly sloppy notation (because there is no full geometric equivalency) and define $\langle 100\rangle = \{[100], [\bar{1}00]\}$ and $\langle 010\rangle = \{[010], [0\bar{1}0]\}$, and $\langle 110\rangle = \{[110], [\bar{1}10], [1\bar{1}0], [\bar{1}\bar{1}0]\}$.

Table 1. Edge energy δ in eV/Å from the different type of edges using the simple bond-counting model (see text) with $E_{\text{bond}} = \frac{2}{3}E_{\text{coh}}$ and three flavours of DFT calculations (see text).

	$\delta_{\langle 100\rangle}$ (ZZSe/ZZSn)	$\delta_{\langle 010\rangle}$ (A)	$\delta_{\langle 110\rangle}$ (ASn/ASe)
bond-counting model	0.256	0.500	0.357
DFT (non opt.)	0.231	0.177	0.141
DFT (partially opt.)	0.137	0.089	0.079
DFT (fully opt.)	0.102	0.088	0.058

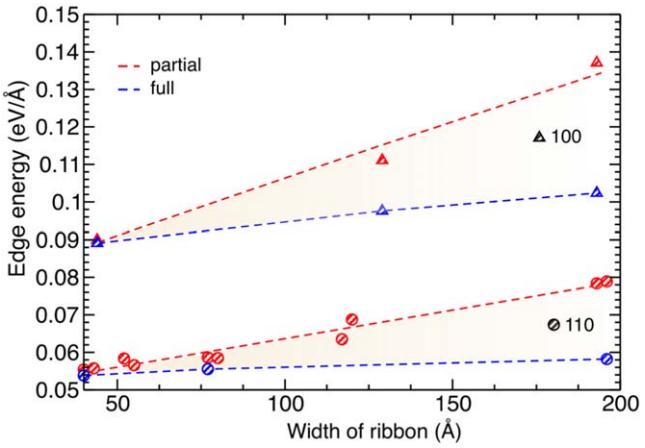

Figure 5. Dependence of the edge energy δ on the width of the SnSe ribbon. The results are compared for different optimization methods i.e. with ('full') or without ('partial') relaxation of the lattice constant perpendicular to the edge.

We find that the islands are dominantly bounded by edges perpendicular to $\langle 110\rangle$. This allows us to determine the island orientation also in large-scale images as 4 (a). We can observe islands in all three orientations (one example for each orientation is highlighted) that are equally distributed across the sample.

From our experimental finding that the island edges are always perpendicular to $\langle 110\rangle$, it directly follows that the equilibrium shape is a parallelogram. Combined with the mirror symmetry of the lattice (and hence the equilibrium shape) with respect to [100] this leads to a rhombus. This also means that the ambiguity in pinning down the specific edge type is not a big problem as in the rhombus even edges of different types have the same length. The rounded corners of the rhombus could be either due to entropy or secondary facets in the equilibrium shape. The fact that zigzag edges are largely absent from the equilibrium shape indicates that the edge-effect on polarization in this system is most probably small.

At first sight, the formation of $\langle 110\rangle$-edges is surprising: In the most simple picture, the edge energy δ is given by the energy E_{bond} needed to break an Se-Sn bond divided by the distance between two broken bonds along the edge. As can be seen in figure 1, this bond-counting model leads to $\delta_{\langle 100\rangle} = E_{\text{bond}}/(2b) \approx E_{\text{bond}}/(2a)$, $\delta_{\langle 010\rangle} \propto E_{\text{bond}}/a$ and $\delta_{\langle 110\rangle} \propto E_{\text{bond}}/\sqrt{a^2+b^2} \approx E_{\text{bond}}/(\sqrt{2}\,a)$ (see also table 1). In consequence, the $\langle 100\rangle$-edges are expected to be energetically the cheapest ones and should dominate the equilibrium island shape. However, it is well known that for 2DMs relaxation (changes of bond lengths and bond angles that conserve the periodicity of the perfect infinite structure) and reconstruction (changes that alter the periodicity) of edges are efficient mechanisms to reduce edge energy [33–36]. For example in graphene, these effects reduce the energy of the ZZ edge by 36% with respect to the bond-counting model and therefore even change the preferred edge type [37, 38]. This motivated us to study the edges of SnSe using DFT.

For the relaxed structure of the infinite lattice (as shown in figure 1) we obtain the lattice constants $a = 4.39$ Å and $b = 4.29$ Å, and the cohesive energy $E_{\text{coh}} = -3.29$ eV/atom. Our calculations show a spontaneous polarization of 0.11 C/m^2 along [100]. These results agree with previous calculations [15, 39, 40]. Furthermore, the structural parameters agree with our experimental results.

We obtained the edge energy by calculating the energy of a finite width ribbon with the particular types of the edges. The ribbons were infinite in the direction of the edges. Due to the low symmetry of the lattice, the ribbons that we calculated ($\langle 100\rangle$, $\langle 010\rangle$, and $\langle 110\rangle$) contain all five different dense-packed edges. Note that in such a low-symmetry lattice and ribbon geometry it is impossible to define the edge energy of a single given edge, only the average energy of a pair related by symmetry can be determined [21].

We found that $\delta_{\langle 110\rangle} < \delta_{\langle 010\rangle} < \delta_{\langle 100\rangle}$, in agreement with our experimental observation. The exact energies, however, strongly depend on the details of our theoretical model, as exemplified in figure 5 for $\langle 100\rangle$- and $\langle 110\rangle$-ribbons. We used different widths of the ribbons (between ≈40 and ≈200 Å) and either allowed a full optimization of the supercell or only a partial optimization where the lattice parameter perpendicular to the edge is restricted to the value found for the 2D infinite lattice. We assume that the partial optimization gives an upper bond for the edge energy, while the full optimization yields a lower bond.

As expected, edge energies for the fully optimized model are lower. More interesting is the dependence on ribbon width: The edge energy increases with width for both $\langle 100\rangle$ and $\langle 110\rangle$, $\langle 010\rangle$ (not shown) behaves analogously. We emphasize that our primary goal is to assess the difference between the edge formation energies of various types since the edge energy values converge very slowly with the ribbon width.

The reason for the slow convergence is that even for the widest ribbons the atomic positions relax throughout the whole system, not only at the edges. Roughly speaking, the atoms are slightly shifted out of their equilibrium position towards the positions they would obtain in the paraelectric phase. We periodically repeated a unit cell found in the middle of the widest fully optimized $\langle 110\rangle$-ribbon. For the resulting 2D infinite lattice structure, we found an energy

which is only 2 meV per unit cell larger than the 2D infinite equilibrium lattice. This energy gain is very small compared with the reduction in energy due to relaxation, explaining the tendency of the ribbons to relax throughout their full width. At some critical width this energy gain would still be too large, and the interior of the ribbon should convert to the equilibrium structure. However, this only happens for very wide ribbons which are beyond the limit of our computational resources.

This finding is in line with extensive studies of the potential energy landscape of free-standing SnSe under systematic variation of the lattice parameters a and b [41], where an energy difference between the ferroelectric ground state and the paraelectric transition state of ≈13 meV per unit cell was found. This is the maximum in energy gain due to distortion, and it is still small compared to the reduction by edge relaxation. This means that for a system like SnSe which is close to a phase transition, a ribbon in the computational model is willing to pay the energetic penalty to transform towards the paraelectric phase when at the same time it can thereby lower its edge energy. The competing energies can be of the same magnitude in such a system. The effect is most pronounced for the narrowest ribbons.

In a recent paper a detailed analysis of the atomic positions in bulk SnSe was performed through the dynamic order-disorder phase transitions [42]. The authors conclude that the potential energy surface is rather flat and may even contain additional local minima. This can further explain the tendency for our ribbons to relax throughout their full width, as the energy penalty for this should be low.

We can exclude that the islands in our experiment globally transform towards the conventional paraelectric phase with its square lattice, as we clearly observe $a \neq b$. We assume that the values derived from the widest ribbons are the most reliable ones and list them in table 1. The large reduction in energy of up to 80 % between the simple bond-counting model and the DFT calculation emphasize the important role of relaxation in this system.

We use the values for the widest ribbons in full optimization for a theoretical prediction of the equilibrium shape. For the full derivation using the Wulff construction we need $\delta(\phi)$, i.e. the edge energy in all directions (delta-plot). The resulting equilibrium shape is still uniquely defined even if the energy is only defined for a pair of edges [21]. We model less densely packed edges as alternating segments of the three main directions as described in supplementary section 5 of [21]. Once $\delta(\phi)$ is defined, the equilibrium shape can be determined by a Wulff construction, which is the geometrical interpretation of the Wulff theorem [43]: to acquire the equilibrium shape from the delta plot, for each point of the curve a line perpendicular to the radius vector at this point is drawn. The resulting inner envelope of all lines is then geometrically equivalent to the equilibrium shape [19]. We find that the ⟨110⟩-edges with the lowest energy dominate the equilibrium shape. This shape is in agreement with our experimental results, as presented in figure 4(b). The corners of the islands are rounded which is not the case in our Wulff construction. The likely reason for that is the neglect of entropy effects in our model. This does not change the fact that the ⟨110⟩ edge is the primary shape defining element.

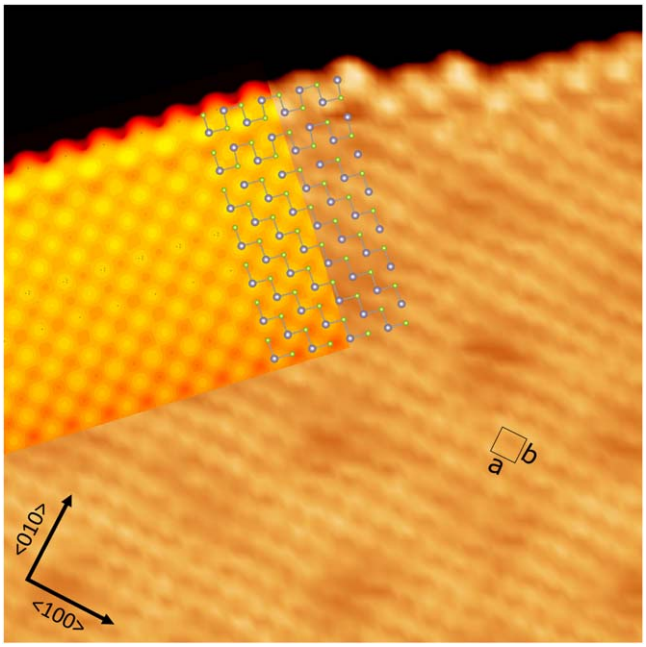

Figure 6. Atomically resolved STM image of SnSe island with edge relaxation in ⟨110⟩ direction; 100 Å × 100 Å, 1 V, 200 pA, grown at 5.2×10^{-3} ML s^{-1} for 60 s at RT and 1.72×10^{-3} ML s^{-1} for 300 s at 570 K. In the top left, a simulated STM image is superimposed. In the middle, the atomic structure obtained by DFT is superimposed on both experimental and simulated STM image (only topmost atoms included).

The dependence of the edge energy on ribbon width and boundary conditions is not critical for the prediction of the equilibrium shape, as here the decisive parameter is the ratio of energies. These stay approximately the same when comparing between a group of ribbons with the same widths and the same optimization.

Recent calculations also found a preference for the ⟨110⟩-edges [21]. In this study, only very narrow ribbons with a width of ≈20 Å were studied, for which there is also quantitative agreement with our energies for the narrowest ribbons represented in figure 5.

In STM experiments we observe an edge relaxation in the ⟨110⟩ edge as shown in figure 6. Since we do not see a difference between ⟨110⟩ edges only one example is shown. When one follows atomic rows parallel to the edge, one can observe that their spacing perpendicular to the edge increases by 6 % comparing the interior of the island with the last two rows at the edge. The edge itself also appears brighter in STM.

Our DFT model also finds an increased row distance at the edge which is in turn mostly compensated by the first and third row. Furthermore, we simulated the STM image of the edge and can reproduce the bright contrast at the edge followed by a darker gap (see overlay in figure 6). Taken together, the agreement between experiment and theory confirms our model of edge relaxation.

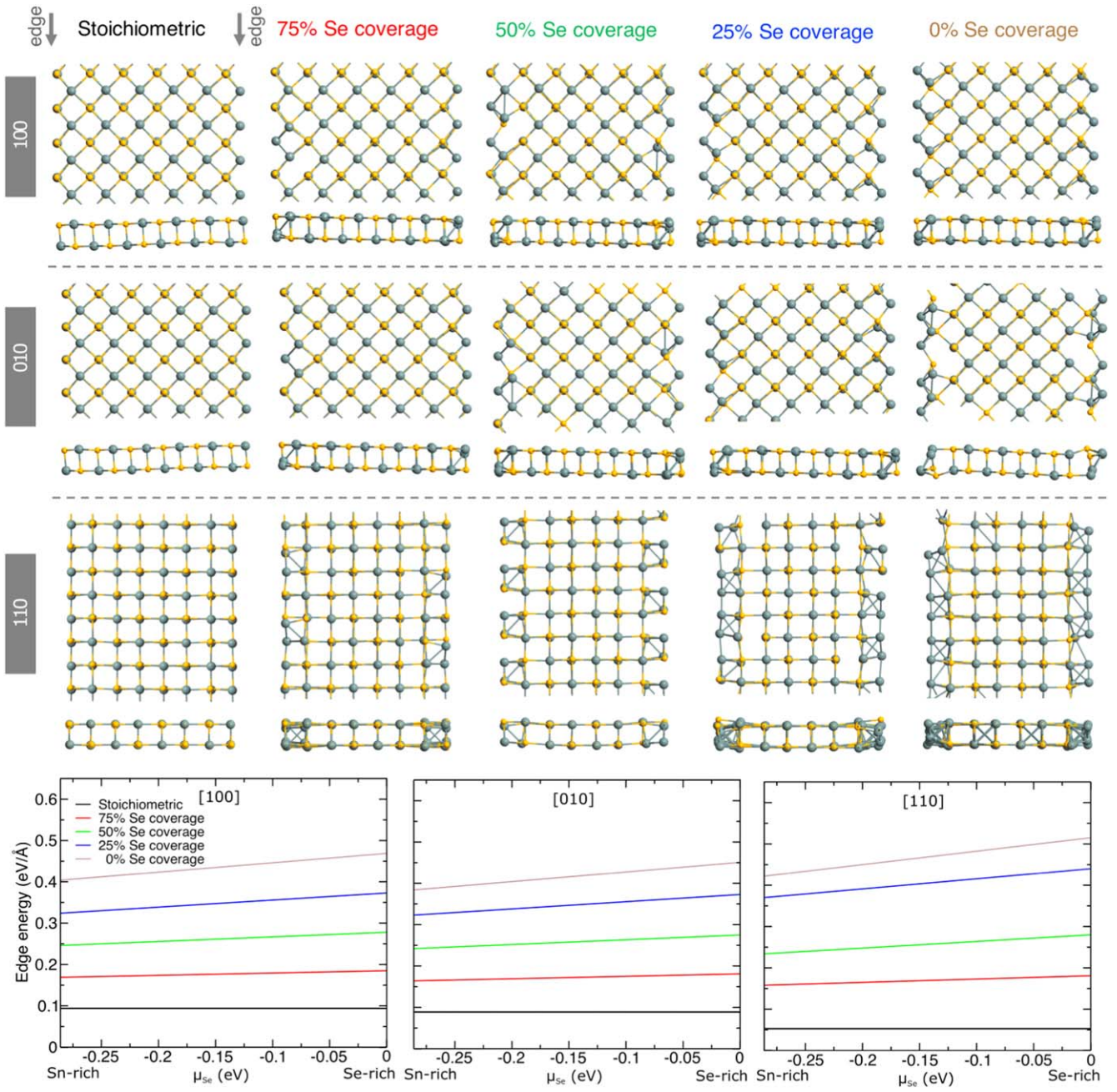

Figure 7. Atomic structures and edge energies δ of stoichiometric and non-stoichiometric SnSe edges as functions of Se chemical potentials.

A way to assess the importance of the ionic bonds in the significant reduction in edge energy upon relaxation would be a comparison with the isostructural material phosphorene, where only covalent bonds are present. Unfortunately, in previous work [34] only the edges corresponding to $\langle 100 \rangle$ and $\langle 010 \rangle$ have been studied. For these, the energy gain due to relaxation and reconstruction was maximum 26 % in comparison to the bond-counting model.

As an alternative to evaporation from SnSe powder using a single source used by us, thin films of SnSe have also been grown by co-evaporation of Sn and Se using two effusion cells [44, 45]. This method is in principle also applicable for the growth of monolayers. It allows to tune the fluxes of Sn and Se independently from each other. The studies mentioned above found that even for significant deviations from the ideal 1:1 flux ratio, stoichiometric thin films of SnSe are formed. However, it can be expected that the Sn:Se ratio at the edges deviates from the 1:1 bulk ratio.

In order to estimate the stability of various edge orientations and terminations also for non-stoichiometric edges, the edge energies were calculated as functions of Se-chemical potential, as shown in figure 7. Depending on the Se concentrating at the edge, several edge compositions were considered where 100 % Se coverage indicates the stoichiometric edge and the other Se deficient edges are non-stoichiometric. In contrast to the stoichiometric edges, for the non-stoichiometric ones for several cases also a change in periodicity, i.e. a relaxation takes place. Regarding energetics, first of all, the

edge energy for stoichiometric ⟨110⟩ edges is lower than for the non-stoichiometric edges over the wide range of the Se chemical potential. Secondly, the edge energy of the stoichiometric ⟨110⟩ edge is lower than that for ⟨100⟩ and ⟨010⟩ edges and thus their presence should be expected. This indicates that equilibrium shapes similar to the one experimentally observed by us should also be found for small deviations from the ideal stoichiometry.

5. Conclusion

We studied the shape of monolayer SnSe islands prepared by MBE on gr/Ir(111). Evaporation at RT leads to the formation of fractal-dendritic islands, indicating that step-edge diffusion is hampered. Annealing does neither lead to Ostwald ripening nor to Smoluchowski ripening before the islands start to desorb at temperatures around 600 K. However, step edge diffusion becomes activated already well before desorption, leading to compact rhombic islands. A two-step process of nucleation of SnSe islands at RT and further deposition at elevated temperature leads to well-formed large islands that are epitaxially aligned with the substrate. We propose that such a two-step process could also be suitable for the growth of large, aligned and well ordered islands of other 2D materials.

In our system, the islands are dominantly bound by edges perpendicular to ⟨110⟩-direction (armchair-like). We interpret the resulting shape as the equilibrium shape. The preference of these particular edges is unexpected in a simple bond-counting model, but can be rationalized by edge relaxations as found in our DFT calculation. We find that a full theoretical description of the edge energies is hampered because the system is close to the ferroelectric-paraelectric phase transition and consequently has a shallow potential energy landscape. Still, our calculations allow a Wulff-construction leading to an equilibrium shape that agrees with the experiment. Atomically resolved images of the dominant edges reveal a relaxation that agrees with the theoretical prediction. Our calculations can be extended beyond the stoichiometric case to predict the edge energies also for related growth methods.

Our insights into atomic processes during epitaxial growth can contribute to a rational choice of preparation parameters to tailor island shapes and sizes. The determination of the preferred edge structure in equilibrium will be relevant for future studies of the ferroelectric properties of SnSe monolayer islands.

Acknowledgments

We acknowledge funding from the German Research Foundation (DFG): Projects KR 4866/9-1, BU 2197/9-2, the collaborative research center 'Chemistry of Synthetic 2D Materials' SFB-1415-417590517, and project 423 876 021 within SPP 2196. TC was supported by the Alexander von Humboldt Foundation. The computational support from the Technical University of Dresden computing cluster (TAURUS) and the High Performance Computing Center (HLRS) in Stuttgart, Germany, is gratefully appreciated.

Data availability statement

The data cannot be made publicly available upon publication because they are not available in a format that is sufficiently accessible or reusable by other researchers. The data that support the findings of this study are available upon reasonable request from the authors.

ORCID iDs

P Aleksa https://orcid.org/0009-0009-8033-6527
M Ghorbani-Asl https://orcid.org/0000-0003-3060-4369
T Chagas https://orcid.org/0000-0001-5688-5985
A Krasheninnikov https://orcid.org/0000-0003-0074-7588
C Busse https://orcid.org/0000-0001-5522-0578

References

[1] Gomes L C and Carvalho A 2020 *J. Appl. Phys.* **128** 121101
[2] Chowdhury C, Karmakar S and Datta A 2017 *J. Phys. Chem.*C **121** 7615
[3] Bao Y *et al* 2019 *Nano Lett.* **19** 5109
[4] Chang K *et al* 2016 *Science* **353** 274
[5] Barraza-Lopez S, Fregoso B M, Villanova J W, Parkin S S and Chang K 2021 *Rev. Mod. Phys.* **93** 11001
[6] Sutter E, Huang Y, Komsa H-P, Ghorbani-Asl M, Krasheninnikov A V and Sutter P 2016 *Nano Lett.* **7** 4410
[7] Liu H, Neal A T, Zhu Z, Luo Z, Xu X, Tománek D and Ye P D 2014 *ACS Nano* **8** 4033
[8] Wu M and Zeng X C 2016 *Nano Lett.* **16** 3236
[9] Hanakata P Z, Carvalho A, Campbell D K and Park H S 2016 *Phys. Rev.*B **94** 035304
[10] Fei R, Kang W and Yang L 2016 *Phys. Rev. Lett.* **117** 097601
[11] Mehboudi M, Fregoso B M, Yang Y, Zhu W, Van Der Zande A, Ferrer J, Bellaiche L, Kumar P and Barraza-Lopez S 2016 *Phys. Rev. Lett.* **117** 246802
[12] Chang K and Parkin S S 2020 *J. Appl. Phys.* **127** 220902
[13] Shen H, Liu J, Chang K and Fu L 2019 *Phys. Rev. Appl.* **11** 024048
[14] Li F, Wang H, Huang R, Chen W and Zhang H 2022 *Adv. Funct. Mater.* **32** 2200516
[15] Chang K, Küster F, Miller B J, Ji J R, Zhang J L, Sessi P, Barraza-Lopez S and Parkin S S 2020 *Nano Lett.* **20** 6590
[16] Higashitarumizu N, Kawamoto H, Lee C J, Lin B H, Chu F H, Yonemori I, Nishimura T, Wakabayashi K, Chang W H and Nagashio K 2020 *Nat. Commun.* **11** 1
[17] Van Gastel R, N'Diaye A T, Wall D, Coraux J, Busse C, Buckanie N M, Meyer Zu Heringdorf F J, Horn Von Hoegen M, Michely T and Poelsema B 2009 *Appl. Phys. Lett.* **95** 121901
[18] Van Efferen C, Murray C, Fischer J, Busse C, Komsa H-P, Michely T and Jolie W 2022 *2D Mate.* **9** 025026
[19] Michely T and Krug J 2004 *Islands, Mounds and Atoms (Springer Series in Surface Sciences)* (Springer) vol 42
[20] Rabe K M, Dawber M, Lichtensteiger C, Ahn C H and Triscone J M 2007 *Top. Appl. Phys.* **105** 1

[21] Wang L, Shirodkar S N, Zhang Z and Yakobson B I 2022 *Nat. Comput. Sci.* **2** 729
[22] N'Diaye A T, Coraux J, Plasa T N, Busse C and Michely T 2008 *New J. Phys.* **10** 43033
[23] Horcas I, Fernández R, Gómez-Rodríguez J M, Colchero J, Gómez-Herrero J and Baro A M 2007 *Rev. Sci. Instrum.* **78** 013705
[24] Kresse G and Furthmüller J 1996 *Phys. Rev.*B **54** 11169
[25] Kresse G and Joubert D 1999 *Phys. Re.*B **59** 1758
[26] Perdew J P, Burke K and Ernzerhof M 1996 *Phys. Rev. Lett.* **77** 3865
[27] Okazaki A and Ueda I 1956 *J. Phys. Soc. Jpn.* **11** 470
[28] Coraux J, N'Diaye A T, Engler M, Busse C, Wall D, Buckanie N, Meyer Zu Heringdorf F J, Van Gastel R, Poelsema B and Michely T 2009 *New J. Phys.* **11** 023006
[29] Silva C C, Cai J, Jolie W, Dombrowski D, Farwick Zum Hagen F H, Martínez-Galera A J, Schlueter C, Lee T L and Busse C 2019 *J. Phys. Chem.*C **123** 13712
[30] Pielić B, Hall J, Despoja V, Šrut Rakić I, Petrović M, Sohani A, Busse C, Michely T and Kralj M 2020 *J. Phys. Chem.*C **124** 6659
[31] Hall J, Pielić B, Murray C, Jolie W, Wekking T, Busse C, Kralj M and Michely T 2018 *2D Mater.* **5** 025005
[32] Frezza F *et al* 2023 *J. Phys. Condens. Matter* **35** 335001
[33] Sang X, Li X, Zhao W, Dong J, Rouleau C M, Geohegan D B, Ding F, Xiao K and Unocic R R 2018 *Nat. Commun.* **9** 1
[34] Masih Das P *et al* 2016 *ACS Nano* **10** 5687
[35] Liang L, Wang J, Lin W, Sumpter B G, Meunier V and Pan M 2014 *Nano Lett.* **14** 6400
[36] Liu Y, Shang X, Zhuang J, Li D and Cui T 2022 *J. Phys. D: Appl. Phys.* **55** 414003
[37] Zhang Z, Kutana A and Yakobson B I 2015 *Nanoscale* **7** 2716
[38] Koskinen P, Malola S and Häkkinen H 2008 *Phys. Rev. Lett.* **101** 115502
[39] Kamal C, Chakrabarti A and Ezawa M 2016 *Phys. Rev.*B **93** 125428
[40] Deb A K and Kumar V 2017 *Phys. Status Solidi*B **254** 1600379
[41] Barraza-Lopez S, Kaloni T P, Poudel S P and Kumar P 2018 *Phys. Rev.*B **97** 024110
[42] Jiang B, Neu J, Olds D, Kimber S A J, Page K and Siegrist T 2023 *Nat. Commun.* **14** 3211
[43] Wulff G 1901 *Z. Kristallogr.—Cryst. Mater.* **34** 449
[44] Nguyen V Q *et al* 2020 *J. Alloys Compd.* **840** 155680
[45] Chin J R *et al* 2023 *Nanoscale* **15** 9973